Aerodynamic Performance and Interaction Effects of Circular and Square Ducted Propellers

Mourão Bento, Hugo; de Vries, Reynard; Veldhuis, Leo

DOI
10.2514/6.2020-1029

Publication date
2020

Document Version
Final published version

Published in
AIAA Scitech 2020 Forum

Citation (APA)
Mourão Bento, H., de Vries, R., & Veldhuis, L. (2020). Aerodynamic Performance and Interaction Effects of Circular and Square Ducted Propellers. In *AIAA Scitech 2020 Forum: 6-10 January 2020, Orlando, FL* (pp. 1-21). Article AIAA 2020-1029 (AIAA Scitech 2020 Forum). American Institute of Aeronautics and Astronautics Inc. (AIAA). https://doi.org/10.2514/6.2020-1029

AIAA SciTech Forum
6-10 January 2020, Orlando, FL
AIAA Scitech 2020 Forum

10.2514/6.2020-1029

Aerodynamic Performance and Interaction Effects of Circular and Square Ducted Propellers

Hugo F. M. Bento*, Reynard de Vries† and Leo L. M. Veldhuis‡
Delft University of Technology, Delft, 2629 HS, The Netherlands

Ducted propellers constitute an efficient propulsion-system alternative to reduce the environmental impact of aircraft. These systems are able to increase the thrust-to-power ratio of a propeller system by both producing thrust and by lowering tip losses of propellers. In this research, steady and unsteady RANS CFD simulations were used to analyze the possible impact of modifying a propeller duct shape from a circular to a square geometry. Initially, the two duct designs and the propeller were studied separately, in order to estimate the numerical errors and to compare with existing data. In the installed simulations, the propeller was first modelled as an actuator disk, and afterwards with a full blade model, in order to understand the time-averaged influence of the propeller on the duct before studying the complete unsteady propeller-duct interaction. In the current design, the square duct corners were found to be prone to separation, and to contribute towards the generation of strong vortices. Furthermore, due to the reduced leading-edge suction on the square duct, the square ducted system was found to be 4.5% less efficient than the circular one, for the conditions tested. By relating the aerodynamic interaction phenomena to the performance of the system, this study provides and important basis for the design of unconventional ducted systems.

Nomenclature

AR = aspect ratio, D/c
B = number of blades
c = chord [m]
C_d = sectional drag coefficient
C_D = drag coefficient, $D/(q_\infty S_p)$
C_f = skin friction coefficient, τ_w/q_∞
C_p = pressure coefficient, $(p - p_\infty)/q_\infty$
C_ω = vorticity coefficient $C_\omega = \omega/(2\Omega)$
D = drag [N], diameter [m]
h_i = average cell size of mesh i [m]
J = advance ratio, $V_\infty/(n\,D)$
k = turbulent kinetic energy [m^2/s^2]
n = angular velocity, $\Omega/(2\pi)$ [rev/s]
P = perimeter [m]
P_{shaft} = shaft power, $Q\Omega$ [W]
p = observed order of convergence of the fit, static pressure [Pa]
q = dynamic pressure [Pa]
Q = torque [Nm]
Q_c = torque coefficient, $Q/(q_\infty\,S_{\text{p}}\,R_{\text{p}})$
r = radial coordinate [m]
R = convergence ratio, radius [m]
Re$_c$ = chord-based Reynolds number
S_{p} = propeller disk area [m^2]
T = thrust [N]
T_c = thrust coefficient, $T/(q_\infty\,S_{\text{p}})$
U_ϕ = uncertainty for quantity ϕ
U_s = standard deviation of the fit
V = velocity [m/s]
x, y, z = Cartesian coordinates [m]
α = angle of attack [deg]
β = blade pitch [deg]
δ_{RE} = error relative to estimated exact solution
Δ_{M} = maximum difference between solutions
ζ = generic quantity
η = system efficiency, $V_\infty(T_{\text{p}} + T_{\text{duct}})/P_{\text{shaft}}$
η_{p} = propeller efficiency, $V_\infty T_{\text{p}}/P_{\text{shaft}}$
θ = azimuthal location [deg]
τ_w = skin friction [Pa]
ϕ = spanwise location
ω = specific dissipation rate [s^{-1}], vorticity [s^{-1}]
Ω = angular velocity of the propeller [rad/s]

Additional sub- and superscripts

1B = loads per blade
AD = actuator-disk model
b = blade
p = propeller
FB = full-blade model
∞ = free-stream conditions
$*$ = value relative to theoretical order of convergence

---

*PhD Candidate, Wind Energy Section, Faculty of Aerospace Engineering, H.F.MouraoBento@tudelft.nl, AIAA Member.

†PhD Candidate, Flight Performance and Propulsion Section, Faculty of Aerospace Engineering, R.deVries@tudelft.nl, AIAA Member.

‡Full Professor, Flight Performance and Propulsion Section, Faculty of Aerospace Engineering, AIAA Member

I. Introduction

In recent years, the motivation to reduce the environmental footprint of air travel has raised the importance of propeller research. With the goal of further increasing propellers efficiency and potentially reduce community noise, ducts can provide several advantages. Ducts are able to produce thrust [1, 2] and to lower the tip losses of propellers [3, 4]. Literature indicates that the advantages of ducting a propeller are most noticeable at low free-stream Mach numbers [1], when the propeller causes a stronger slipstream contraction. Furthermore, ducts can increase the safety and, according to Hubbard [5], decrease noise emissions of propellers. With all their advantages, ducted propeller systems have also been appealing for rather unconventional aircraft designs. One example is the low-wing aircraft with fuselage mounted ducted propellers (FMDP) studied in Ref. [6]. The FMDP aircraft uses a propulsive empennage, as the two ducted propellers present at the aft fuselage are also responsible for providing control and stability. Ducted rotor systems have also gained significant interest in recent years in the field of (hybrid-electric) distributed propulsion [7, 8]. Hybrid-electric aircraft concepts employing distributed ducted systems include over-the-wing [9], under-the-wing [10], and boundary-layer ingesting [11] configurations, as well as several urban air mobility concepts [12].

However, despite the strong influence of the design of the ducted propulsion system on the aerodynamic characteristics of the aircraft, the shape of the duct is generally not investigated in conceptual design studies [9, 11], and is only obtained on a case-specific basis through high-fidelity optimizations (see e.g. Ref. [10]) later in the design process. This is mainly because, in a broader sense, it is unclear what the optimal duct shape is for a generic propulsion-system arrangement. Although the circular duct is the most obvious candidate due to the axisymmetric nature of the rotors, more unconventional ducts may present additional aerodynamic or structural advantages. To provide an example, Fig. 1 shows a notional aircraft concept featuring two distinct ducted propulsion systems: a propulsive empennage, and an over-the-wing distributed-propulsion system. For the propulsive empennage, changing the duct trailing edge from circular to square would allow the placement of control surfaces on the duct edges, thus reducing the size of the stator vanes. For the distributed-propulsion array, multiple duct designs can be envisioned, such as an array of circular ducts, a two-dimensional "envelope" duct, an array of square ducts, or a combination thereof. It is evident that, in this case, the non-circular designs can provide a reduction in wetted area, reduce the structural complexity of the duct, and ease the integration with the rest of the airframe. In all these designs, a fundamental understanding of the aerodynamic interaction between the rotor and the duct is required to be able to predict the aerodynamic performance of the system and to, subsequently, establish design guidelines for these propulsion-system arrangements. The aerodynamic interaction effects present in these unconventional designs can, in turn, be understood by analyzing two simplified limit cases: a circular ducted rotor, and a square ducted rotor (Fig. 1c). However, the studies found in literature regarding the aerodynamic performance of ducted propellers only refer to circular ducts [1–4]. While aerodynamic phenomena present in uninstalled square ducts can, to a certain extent, be inferred from corner flow studies [13, 14], it is unclear how these phenomena are affected by the presence of a rotor. Thus, it is currently difficult to estimate the impact of using a non-axisymmetric duct on the propulsive performance of the system.

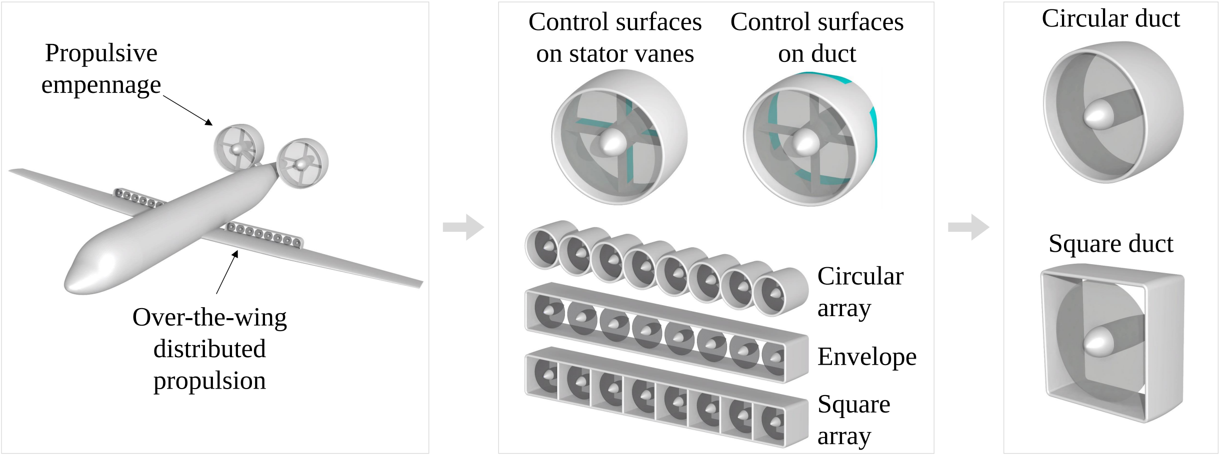

a) Notional aircraft concept **b) Possible propulsion system designs** **c) Limit cases**

Fig. 1 Simplified representation of the ducted propeller systems present in unconventional aircraft designs.

The objective of this study is therefore to analyze the aerodynamic interaction phenomena present in unconventional ducted propeller systems, and to understand how these phenomena affect the performance of the system. Steady and unsteady RANS computational fluid dynamics (CFD) simulations are performed in order to obtain the flow fields of two different ducted propellers. Firstly, a circular duct (or ring wing) is evaluated, in order to provide a reference. Secondly, a square duct is analyzed, since this idealized geometry provides a clearer understanding of the aerodynamic interaction effects present in non-axisymmetric duct designs. A thorough understanding of the differences between these two idealized geometries allows a more efficient design of case-specific ducted propeller systems. The specific duct and propeller geometries considered, as well as the numerical methods used to study their performance, are described in Sec. II. Section III then discusses the uncertainties of the CFD simulations and compares the numerical results with results obtained in other studies. Afterwards, Sec. IV describes the most relevant interaction phenomena observed in the ducted propeller systems. Finally, Sec. V discusses the main effects of the interaction between the propeller and each duct on the aerodynamic performance of the system.

II. Computational Setup

This section describes the main characteristics of the models and numerical methods used during this study. To this end, Sec. II.A presents the geometries employed, Sec. II describes the solver setup, Sec. II.C discusses the two methods used to model the propeller, Sec. II.D presents the domains and boundary conditions used, and finally Sec. II.E discusses the main characteristics of the grids used.

A. Geometry

Two ducted propeller geometries were studied: a circular and a square ducted propeller, shown in Fig. 2. To allow easy reference to studies on 2D airfoils the NACA0012 airfoil is selected for the duct. The ducts have an aspect ratio AR $= D/c = 2$, where D is the diameter of the circular duct, which is equal to the square duct's span. In order to improve the convergence of the simulations, the corners of the square duct were slightly rounded, so that the minimum corner radius (at the airfoils' thickest point) would be 1% of the propeller radius, R_p. The minimum gap between the propeller tips and duct surface (or tip clearance) was maintained at 0.3% of the propeller radius, leading to a duct chord of approximately 0.217 m. The propeller geometry was based on an existing design, denoted "XPROP", that has been characterized previously in both experimental and numerical studies [15–18]. The six-bladed wind-tunnel model has a radius of $R_\text{p} = 0.2032$ m. Details regarding the propeller geometry, such as chord and twist distributions, can be found in Ref. [15]. In this study, the blade pitch for the radial location $r/R_\text{p} = 0.7$, $\beta_{0.7}$, was kept at 30°. The number of propeller blades was reduced to 4 so that only one quarter of the domain had to be solved, using periodic boundary conditions. The axial location of the propeller was set to 30% duct chord, which is the location of maximum thickness of the NACA 0012 airfoil. When placed too far upstream, the propeller might experience a radially less uniform inflow [19]. On the other hand, the propeller also needs to be positioned sufficiently upstream of the duct's trailing edge, if it is intended place control surfaces at the duct's surface, as represented in Fig. 1b. Figure 2 also shows the axis system used, and how the azimuthal location, θ, and the spanwise location, $\phi = l/(4P)$, were defined. l is the length along the duct's span, starting at the top surface's mid-span, and P is the perimeter of the duct. The propeller rotates in counter-clockwise direction when viewed from the front, as indicated by the angular velocity vector Ω in Fig. 2a.

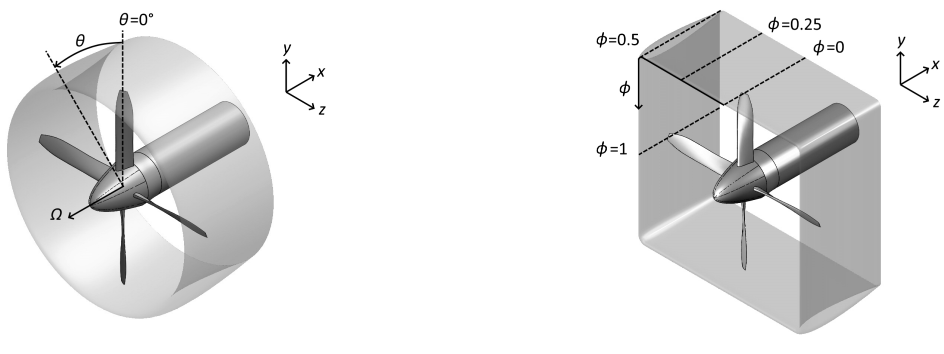

(a) Circular ducted propeller. **(b) Square ducted propeller.**

Fig. 2 Isometric view of the circular and squared ducted propeller's geometries, with definitions of the axes, propeller angular velocity, Ω, azimuthal location, θ, and spanwise location, ϕ.

B. Solver Setup

The CFD simulations were performed using the solver ANSYS Fluent 18.2, and were based on the solution of steady and unsteady RANS equations. The RANS equations were discretized using the 3rd order MUSCL scheme (Monotonic Upstream-centered Scheme for Conservation Laws) [20], which was developed from the original MUSCL scheme (introduced by van Leer [21]). As the solver ANSYS Fluent is cell-centered, the values of pressure at the cell faces were calculated by interpolation considering the values of pressure at the center of the cells [20], with a 2nd order scheme. The unsteady calculations were made using a 2nd order implicit temporal discretization. The simulations of the isolated ducts were made considering the flowfields to be steady, whereas for the computations with the propeller both steady and unsteady flowfields were calculated. The fluid (air) was modelled as an ideal gas in order to take into account compressibility effects.

Furthermore, turbulence was modelled using the two-equation k-ω shear-stress transport (SST) turbulence model, which was developed by Menter [22]. This model has been used previously in several propeller-related studies [23–26]. Besides, the k-ω SST model has been concluded to be relatively accurate for a wide range of flowfield problems, when compared against other one or two equation turbulence models (which yield similar computational costs) [27]. However, the results should be analyzed while keeping in mind that the model also has drawbacks. As an example, the k-ω SST model experiences difficulties at predicting separated flows [28].

C. Propeller Modelling Methods

Two different methods were used to model the propeller: a full blade (FB) model and an actuator disk (AD) model. With the full-blade model, the propeller blade surfaces are included in the simulation, and the boundary layer of the propeller is also calculated. The full blade model was used for the isolated and installed simulations with the propeller. For the isolated propeller computations, both steady and unsteady simulations were performed. The steady simulations were performed using a Multiple Reference Frame approach (MRF), so that the propeller blades remain stationary. The MRF approach is valid when the flowfield is steady is the reference frame of the rotating body (e.g. a propeller). In the unsteady simulation, the rotation of the blades was modelled using a sliding mesh technique. For the ducted propeller installed cases, the FB model was only used to obtain unsteady solutions.

The actuator disk model was used to estimate time-averaged interaction effects, for the installed configurations. The AD model applied in this study was developed at TU Delft, and has been subjected to a validation study in Ref. [29]. The AD imposes an axial momentum, tangential momentum and energy jump at the propeller location, as described in Ref. [29]. Thus, the AD requires the thrust and torque of the propeller as inputs. In this research, the inputs of the AD were obtained from FB simulations of the isolated propeller.

D. Domain and Operating Conditions

The domain used for the simulation of the square ducted propeller is presented (with the FB model) in Fig. 3. This domain is equal to the domain used in the circular ducted propeller simulation. Figure 3a shows that the domain was reduced to one quarter (to a 90° domain) by using periodic boundary conditions. Far upstream of the geometry, the flow direction and the total pressure and temperature were specified at the inlet. The inlet values were calculated in order to result in a free-stream velocity, V_∞, of 30m/s, at sea-level conditions. In the far-field boundary, the flow direction, the static pressure and temperature and the Mach number were specified in order to impose equivalent free-stream conditions. Besides, the free-stream values of turbulent kinetic energy, k_∞, and specific dissipation rate, ω_∞, were specified at the inlet and far-field boundaries. The values of k_∞ and ω_∞ were chosen according to the recommendations of Ref. [30]. The decay of k and ω from the inlet to the studied geometries was avoided by placing sources for these quantities inside the domain, also in agreement with the recommendations found in Ref. [30]. At the outlet, the static pressure was prescribed. Figure 3b shows that the duct surface, the propeller blade and the spinner were modelled as no-slip walls, whereas the remaining part of the nacelle (which was extended until the outlet) was modelled as a free-slip boundary. The remaining simulations were made with similar domains. For the AD simulations, the propeller blade was not included and the spinner was also modelled as a free-slip wall. The inputs for the AD model were obtained from the simulation of the isolated propeller at three operating conditions: $J = 0.7$, $J = 0.8$ and $J = 0.9$. For the simulation of the isolated propeller, the steady simulations were performed with a propeller domain considerably larger (in the radial direction) than the small propeller domain, sPD, shown in 3b. With a sPD, a steady solution calculated with the MRF approach leads to unphysical results [31], and thus only unsteady simulations were performed with the sPD. The FB power-on simulations were performed at an advance ratio of $J = 0.7$, which corresponds to an angular velocity of $\Omega = 663$ rad/s at the V_∞ tested. In the specific case of the computation of the isolated circular duct flowfield, an additional 2D simulation was made, using an axisymmetic boundary condition in the duct's axis. The 2D simulation was used in the verification and validation process of the isolated duct computations.

A summary of the operating conditions considered in this study can be found in Table 2. The free-stream values of density, pressure and temperature, which are omitted in the table, correspond to sea-level conditions. The advance ratio tested in the installed FB simulations, $J = 0.7$, is representative of climb conditions, as this value corresponds to a high thrust setting.

Table 1 Operating conditions used in the uninstalled and installed simulations.

Test case	V_∞ [m/s]	α [°]	k_∞ [m^2/s^2]	ω_∞ [s^{-1}]	$\beta_{0.7}$ [°]	J [-]
Uninstalled ducts	30	0	9×10^{-4}	695	30	-
Uninstalled propeller (FB)						0.9, 0.8, 0.7
Ducted propeller (AD)						0.9, 0.8, 0.7
Ducted propeller (FB)						0.7

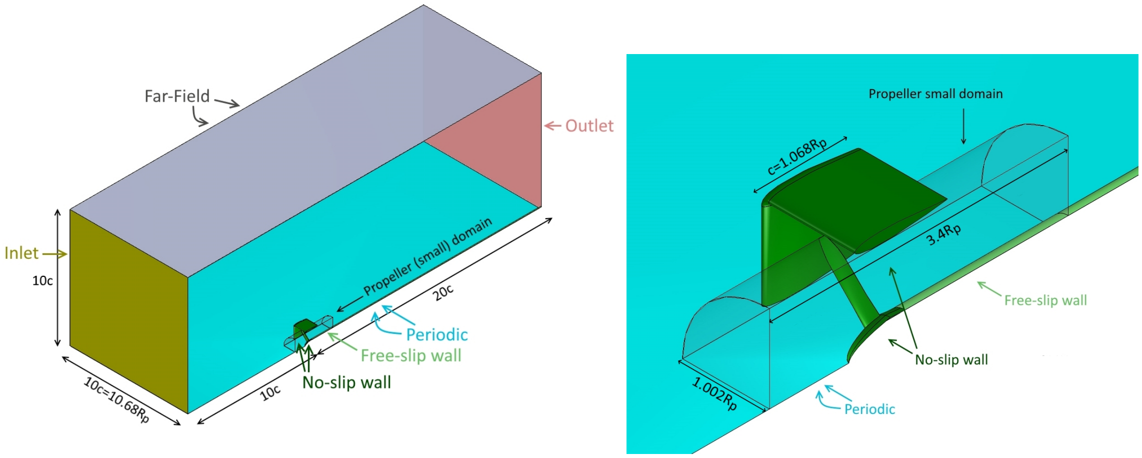

(a) Isometric view of the square ducted propeller simulation domains.

(b) Close up view of the propeller, for the small propeller domain (sPD) case.

Fig. 3 Domains and boundary conditions used for the simulation of the square duct with propeller.

E. Grid

The grids used in this research were generated with ANSYS Meshing software. In most regions, an unstructured mesh was used. However, near no-slip walls, inflation layers were generated. The inflation layers allow for the specification of the first layer height, which was set in all surfaces in order to achieve in a maximum y^+ lower than 1. Besides, the prism shaped inflation layers resemble a structured mesh, allowing the elements to be more aligned with the (expected) main local flow direction. This improves convergence, even though the solver ANSYS Fluent always reads the mesh as unstructured. Furthermore, the surface mesh over no-slip walls was also specified as a structured-like mesh. However, in critical regions, exceptions had to be made and the surface mesh was also set as unstructured. The unstructured surface mesh was used in the square duct's corner and in the regions of the ducts' surface in close proximity to the blade tips. Due to the complexity of the grids generated for the installed configurations with the FB model, the resultant mesh sizes led to large increases in the computational cost of the unsteady installed calculations. The FB circular ducted propeller and the FB square ducted propeller grids had, respectively, 16 and 20 million elements.

III. Uncertainty Quantification and Validation

This section discusses the numerical error in the CFD simulations, as well as the validation of the isolated circular duct and propeller simulations. The numerical discretization error was assessed by performing grid convergence studies, and is discussed in Sec. III.A. The validation was performed by comparing the results of the simulations with experimental results available, in Sec. III.B.

A. Grid convergence study

The numerical discretization error was estimated for the steady simulations of the isolated circular duct, isolated square duct, and isolated propeller. The numerical error of the isolated circular duct computations was estimated for both the 2D axisymmetric and the 3D setups. The discretization error is commonly the strongest source of numerical error in CFD simulations [32]. The discretization error was analysed by a performing grid convergence study for each isolated configuration. The grids were modified by changing the cell size settings in ANSYS meshing software so that each finer or coarser mesh would have the specified refinement ratio with respect to the previous mesh, while keeping all the grids geometrically similar (for each case), as recommended in Ref. [32]. The cell sizings relative to inflation zones were chosen in order to keep the total height of each inflation zone height constant, for the different grids. As the first cell height was also kept constant (in order to maintain the same y^+), the growth rate of the inflation layers had to be modified in order to increase or decrease the number of layers inside each inflation zone.

Table 2 shows, for each grid, the number of elements and the grid refinement ratio with respect to the finest grid, (h_i/h_1). The refinement ratios shown in Table 2 were calculated based on the number of generated cells, and differ from the ratios estimated based on the specified sizings. The differences are assumed to be associated with the grid generation algorithm used by ANSYS meshing. For the square duct and propeller, less grids were considered than for the circular duct, due to convergence issues with the remaining generated grids. Eça and Hoekstra [32] recommend the usage of at least 3 geometrically similar grids, in order to perform a convergence study.

Table 2 Grids used in the convergence studies circular duct, square duct and propeller, in their isolated configurations. "2D*" refers to a two-dimensional (axisymmetric) simulation in cylindrical coordinates.

	2D* Circular duct		3D Circular duct		Square duct		Propeller	
grid	# of cells	h_i/h_1	# of cells	h_i/h_1	# of cells	h_i/h_1	# of cells	h_i/h_1
6	7.92×10^3	2.89	2.32×10^6	1.76	-	-	-	-
5	14.18×10^3	2.16	2.60×10^6	1.70	-	-	-	-
4	19.86×10^3	1.82	3.30×10^6	1.60	5.23×10^6	1.33	-	-
3	28.46×10^3	1.52	4.61×10^6	1.40	7.08×10^6	1.20	4.01×10^6	1.59
2	42.88×10^3	1.24	7.00×10^6	1.22	9.26×10^6	1.10	7.96×10^6	1.27
1	65.95×10^3	1.00	12.71×10^6	1.00	12.34×10^6	1.00	16.18×10^6	1.00

Grids 4, 3, 1, and 2 were selected for the 2D axisymmetric duct, 3D circular duct, square duct, and propeller cases, respectively. Grids 4 and 3, respectively for the 2D and 3D circular duct simulations, have similar cell size settings. The results from the different grids were then used to estimate the numerical uncertainty based on the method described in Ref. [32]. The method was adapted for the 3rd order discretization scheme used in this study. Thus, the theoretical order of convergence of the studied quantities was assumed to be 3. Considering this difference, the numerical uncertainty, U_ζ, relative to the calculation of a given quantity ζ was estimated from:

$$U_\zeta = \begin{cases} 1.25\delta_{RE} + U_s & \text{for } 0.95 < p < 3.05 \\ \min(1.25\delta_{RE} + U_s, 1.25\Delta_\mathrm{M}) & \text{for } 0 < p < 0.95 \\ \max(1.25\delta^*_{RE} + U^*_s, 1.25\Delta_\mathrm{M}) & \text{for } p > 3.05 \\ 3\Delta_\mathrm{M} & \text{for } p < 0 \text{ or oscillatory)} \end{cases} \tag{1}$$

where δ_{RE} is the difference between the estimated exact solution and the solution obtained with the considered grid, U_s is the standard deviation of the fit, p is the observed order of convergence of the quantity and Δ_M is the maximum difference between all the solutions obtained. δ^*_{RE} and U^*_s are relative to the fits obtained considering p to be equal to the theoretical order of convergence. The quantities analysed during the convergence study were the drag coefficient, C_D, for the isolated ducts, and the thrust, T_c, and torque, Q_c, coefficients for the isolated propeller. The fits obtained for the duct and propeller cases can be seen in Figs. 4, 5 and 6. Table 3 shows the values of the observed order of convergence, standard deviation of the best fit and fit with $p = 3$, and the overall uncertainties calculated from each convergence study. For the propeller case, the convergence ratio $R = (\zeta_2 - \zeta_1)/(\zeta_3 - \zeta_2)$, is also shown. For each case, the standard deviation and the overall uncertainties are shown as a percentage of the value corresponding to the grid which was finally selected.

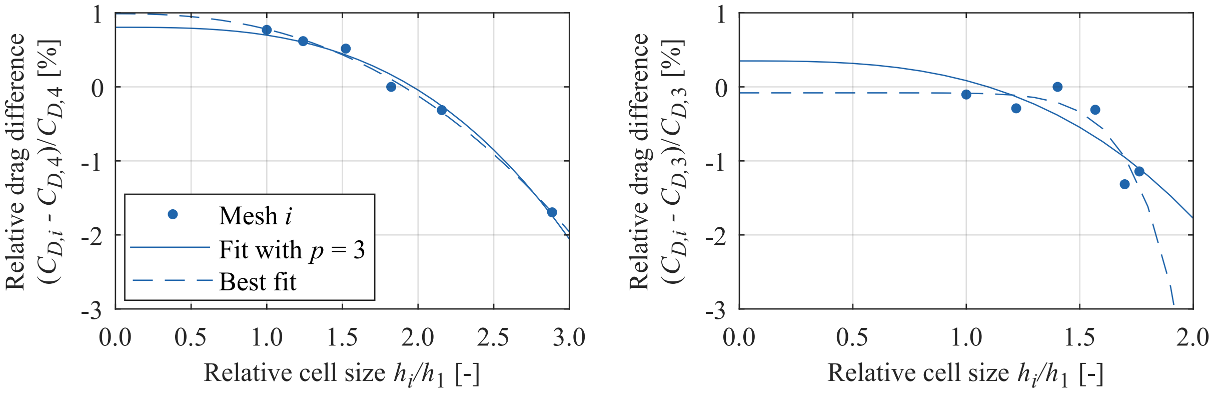

a) 2D circular duct

b) 3D circular duct

Fig. 4 Circular duct grid convergence study.

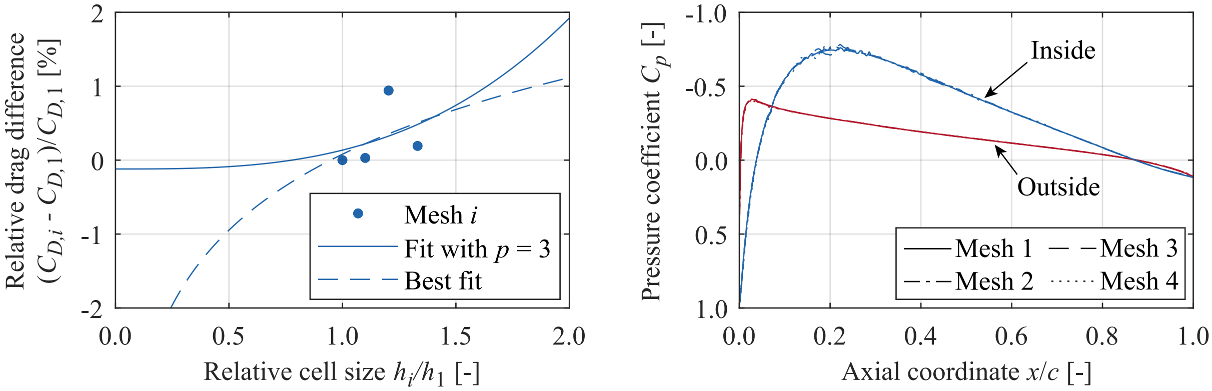

a) Drag convergence

b) Corner pressure distributions

Fig. 5 Square duct grid convergence study.

The uncertainties gathered in Table 3 suggest a low discretization error, ranging from 0.1% for propeller loads, to 1%–2% for duct loads. However, when analyzing the convergence of the pressure- and friction-drag components of the ducts separately, these quantities were found to converge in opposite directions, with friction drag increasing and pressure drag decreasing with grid refinement. In fact, the uncertainty-estimation method described above predicted a 25% and 21% uncertainty in pressure drag for the (3D) circular and square ducts, respectively, and a 9.5% and 6.8% uncertainty for the friction drag. Hence, when considering the relative impact of these two drag contributions, the total drag uncertainty would be approximately 13% and 10% for the circular and square ducts, respectively. To verify whether these high uncertainties were the consequence of a poorly resolved flow field or simply an artifact of the uncertainty-estimation method, the pressure distributions on the ducts were monitored, and the 3D circular-duct convergence was compared to the 2D one. For the 2D case, a wider range of cell sizes could be evaluated due to the reduced computational costs, and in this case the pressure drag, friction drag, and total drag all presented low uncertainties. Moreover, the observed order of convergence corresponded closely to the theoretical order of convergence

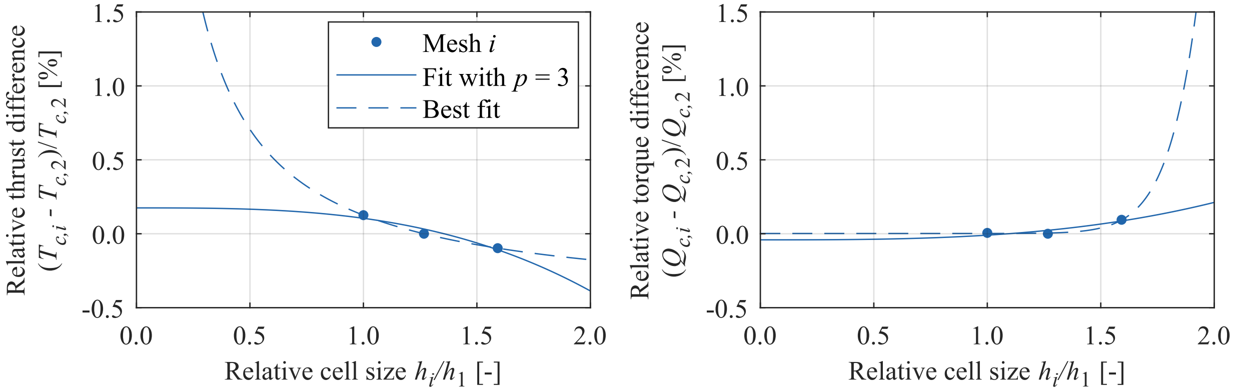

a) Thrust convergence **b) Torque convergence**

Fig. 6 Propeller grid convergence study.

(p = 3), as visible in Fig. 4a. While this was not the case for the 3D circular duct (Fig. 4b), the drag values obtained matched closely with the ones obtained from the 2D case (see Fig. 7), suggesting that the high uncertainties in pressure and friction drag were an artifact of an over-conservative uncertainty estimation. For the 3D square duct, no analogous 2D simulation could be performed, and the observed order of convergence differed considerably from the theoretical one (p = 3), as can be observed in Fig. 5a. However, the pressure distribution over the duct surface was found to be sufficiently converged for the selected grid (Grid 1), as shown in Fig. 5b. The fluctuations visible around $x/c = 0.2$ for the coarser grids were much higher in the corner region, shown in the figure, than along the rest of the duct, due to the unstructured mesh in the corner. Based on these observations, the pressure- and friction-drag uncertainty estimates were considered to be extremely conservative, and thus the overall grid uncertainty was considered acceptable for this study. More details on the convergence study of these grids can be found in Ref. [31].

Table 3 Estimated grid convergence uncertainties for the isolated circular duct, square duct and propeller configurations. "2D*" refers to a two-dimensional (axisymmetric) simulation in cylindrical coordinates.

Quantity	2D* Circular duct	3D Circular duct	Square duct	Propeller	
	C_D	C_D	C_D	T_c	Q_c
p	2.41	9.85	0.015	-0.94	14.96
U_s [%]	0.086	0.30	0.70	0	0.0064
U_s^* [%]	0.12	0.40	0.72	0.040	0.029
R [-]	-	-	-	-0.062	0.89
U_ζ [%]	1.32	1.64	1.18	0.095	0.0088

B. Comparison with experimental studies

In this section, the simulation results are compared to existing experimental data. Although the geometries and operating conditions of these data differ slightly from the ones analyzed in this study, a qualitative comparison is performed to increase the confidence in the numerical results.

1. Isolated circular duct

The estimated values of the circular duct's drag coefficient were compared against results found in literature regarding similar geometries. Figure 7 shows the sectional drag coefficients of a 2D NACA 0012 profile for various Reynolds numbers [33], and the drag coefficient of the circular duct analyzed by Traub [34]—which has the same airfoil and aspect ratio as the one analyzed in this study. The drag coefficients obtained in this study for both the axisymmetric 2D and the 3D simulations are also included. The two CFD solutions show a very good agreement, as expected. The results from the 2D experiments indicate that the sectional drag coefficient, C_d, of the NACA 0012 profile decreases with the chord based Reynolds number, Re_c, from $\mathrm{Re}_c = 0.17 \times 10^6$ to $\mathrm{Re}_c = 0.33 \times 10^6$. In the experimental studies considered [33, 34], the Re_c influences the transition location over the airfoil sections. From $\mathrm{Re}_c = 0.33 \times 10^6$ to $\mathrm{Re}_c = 0.66 \times 10^6$, the C_d of the NACA 0012 airfoil remains almost constant, according to Ref. [33]. Traub also studied the circular duct in the wind tunnel at $\mathrm{Re}_c = 0.17 \times 10^6$. This duct's C_d was expected to be higher than the C_d of the NACA 0012 airfoil at the same Re_c, due to a blockage effect, which is confirmed by Fig. 7. The blockage occurs inside the duct, due to its circular shape, and is increased due to the presence of a support structure in the interior of the duct (experimental setup shown in Ref. [34]). The C_d obtained for the circular duct from CFD is lower than the C_d obtained by Traub. This can be explained considering the higher Re_c in the CFD simulation, as well as the absence of a support structure for the computational problem, which leads to a lower blockage effect. The CFD simulation leads to a higher C_d estimation than the NACA 0012 profile experiments at similar Re_c ($\mathrm{Re}_c = 0.33 \times 10^6$ or $\mathrm{Re}_c = 0.66 \times 10^6$), which is due to the blockage effect which occurs inside the duct.

2. *Isolated propeller*

The only data available for validation of the propeller CFD results consist of experimental data obtained at the Open-Jet Facility (OJF) at Delft University of Technology. These data were provided via internal communication by Sinnige [35], who acquired the data using the same experimental setup as Li [15]. The data consists of thrust and torque measurements, performed with a rotating shaft balance at the same free-stream velocity and advance ratios as the ones tested in the CFD simulations. Several factors can lead to discrepancies between the wind tunnel and CFD results, such as the boundary conditions of an open-jet tunnel, the simplification of the nacelle geometry and boundary conditions in the CFD simulations (see Sec. II), the exclusion of the forces on the spinner in the CFD results, and the turbulence modeling of the computational approach. However, most importantly, the propeller used in the experimental campaign had 6 blades, whereas the propeller used in the CFD computations had its number of blades reduced to 4. Since the thrust produced by a propeller does not scale linearly with the number of blades, the wind-tunnel data could not be compared to the CFD directly. Therefore, the authors decided to compare both high-fidelity results to a lower-order method capable of analyzing different numbers of blades. To this end, the program XROTOR [36] was selected to analyse the performance of the propeller geometries with both 4 and 6 blades. XROTOR is a program based on the lifting line method (LLM). Since XROTOR receives airfoil properties as an input, these were obtained for each radial location using the program XFOIL [37].

The CFD results of the propeller simulation were compared against the wind tunnel and LLM results at $V_\infty = 30 m/s$ for three different advance ratios: $J = 0.7$, $J = 0.8$, and $J = 0.9$. Figure 8 shows the thrust and torque coefficients

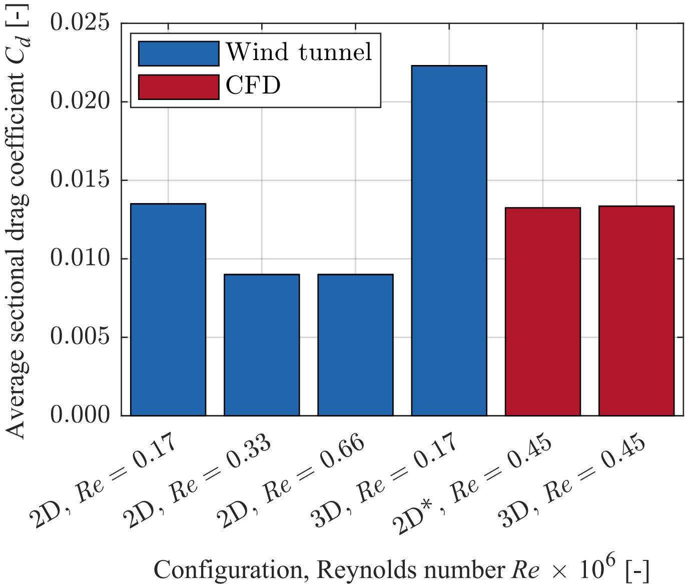

Fig. 7 Comparison of the sectional drag coefficient obtained from CFD with the experimental data of Refs. [33, 34], for a NACA 0012 profile. "2D" = two-dimensional wing in Cartesian coordinates (infinite wing), "2D*" = two-dimensional wing in cylindrical coordinates (ring wing), and "3D" = complete circular duct (ring wing).

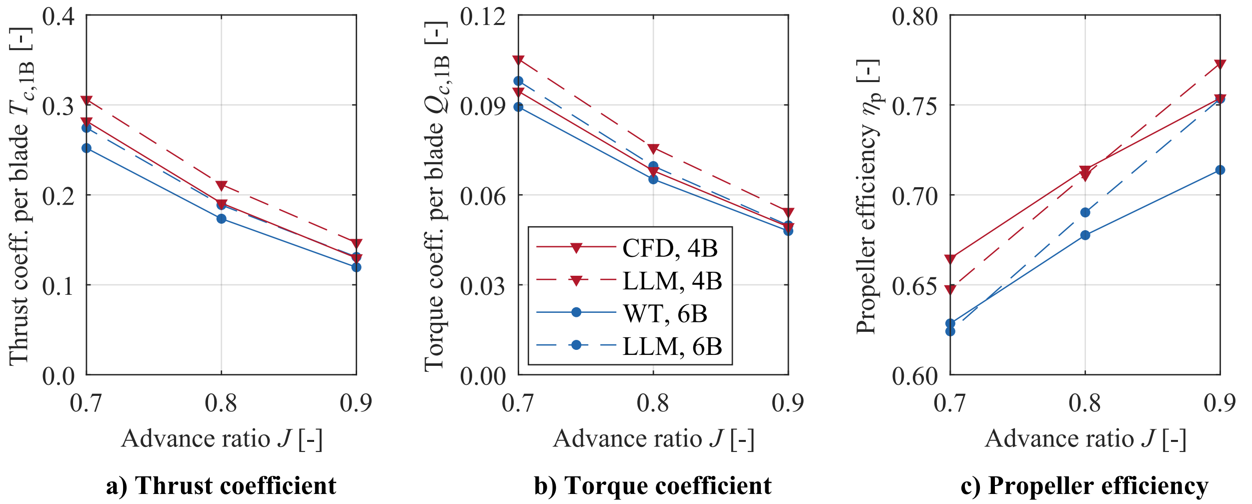

a) Thrust coefficient **b) Torque coefficient** **c) Propeller efficiency**

Fig. 8 Comparison of isolated propeller performance with wind tunnel (WT) data and a lifting-line method (LLM). Note that forces are expressed per propeller blade.

obtained per blade (i.e., $T_{c,1\text{B}} = T_c/B$ and $Q_{c,1\text{B}} = Q_c/B$), as well as the resulting propeller efficiency. When comparing the T_c results of the wind-tunnel experiment with CFD in Fig. 8a, similar trends are observed, although the curves present an offset. The thrust obtained per blade for the 4-bladed (CFD) case is higher than the thrust obtained per blade for the 6-bladed (WT) case, which is expected since a higher total thrust of the 6-bladed propeller leads to a higher induced axial velocity at the propeller disk, and thus to a lower effective angle of attack at each blade section. This can be confirmed by comparing the results obtained for four and six blades using the LLM, which show a comparable offset. The same effect is seen for the torque coefficient (Fig. 8b) and, in both cases, the lifting-line method over-predicts the loads, when compared to the wind tunnel or CFD data. Moreover, the LLM predicts a linear variation of propeller efficiency (Fig. 8c) with advance ratio, while the higher-fidelity methods predict a lower efficiency at high advance ratios. There are several assumptions used in the LLM calculations which may lead to discrepancies with respect to the results obtained with higher fidelity methods; for example, given that XROTOR only accepts a limited number of airfoil characteristics as input, the airfoil polars considered in XROTOR lose accuracy. In any case, the qualitative agreement of the three methods indicates that the isolated propeller performance is captured correctly by the CFD simulations.

IV. Aerodynamic Interaction Phenomena

The following section describes the most relevant aerodynamic phenomena caused by the interaction between the propeller and each duct. First, the circular ducted propeller case is discussed in Sec. IV.A, followed by the square ducted propeller in Sec. IV.B.

A. Circular Duct

Existing literature indicates that a circular duct is able to produce thrust, in the installed configuration, provided that the thrust coefficient, T_c, of the propeller is high enough [1, 2, 19]. A high T_c leads to a higher slipstream contraction of the flow upstream of the propeller. The upstream slipstream contraction causes a change in the effective angle of attack of the duct sections, which then leads to the production of thrust by the duct. To confirm this, the pressure distribution at the surface of the circular duct is evaluated and compared in propeller-on and propeller-off conditions in Fig. 9. Figure 9a indicates that the pressure distribution inside the isolated circular duct is axisymmetric, similarly to the axial skin friction coefficient distribution (Fig. 9b).

The pressure coefficient chordwise distribution for the installed (FB) and uninstalled circular ducts, averaged in the spanwise direction, is shown in Fig. 9c. Figure 9c shows that a strong suction peak occurs at the inner surface of the installed duct, which is indicative of the change in effective angle of attack caused by the propeller. The region of increased suction is maintained up till the location of the propeller, where a sudden increase in static pressure is generated across the propeller disk. Figure 9c also presents the force vectors calculated from the average C_p chordwise

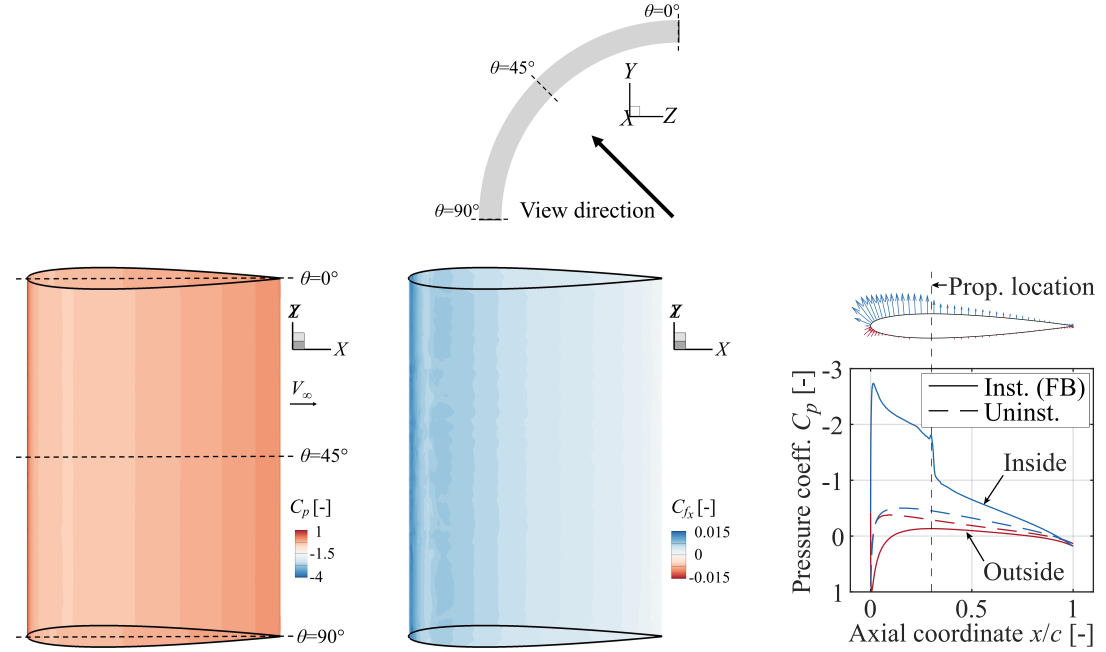

(a) Uninstalled, C_p

(b) Uninstalled, C_{f_x}

(c) Installed and Uninstalled average C_p (bottom), and installed force vectors (top)

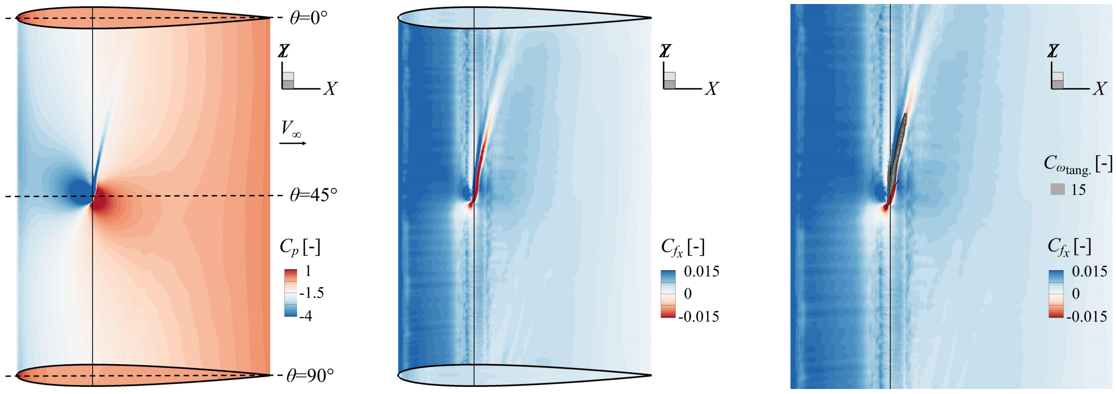

(d) Installed, C_p

(e) Installed, C_{f_x}

(f) Installed, C_{f_x} and $C_{\omega_{\text{tangential}}}$ isosurface.

Fig. 9 Pressure (left) and axial skin friction (center) coefficient contours on the circular duct's inner surface, for the uninstalled and installed cases. The top-right image shows the average chordwise C_p distribution, for the two cases, and the bottom-right image shows a close-up view of the C_{f_x} countours near the blade-tip region, including a tangential-vorticity coefficient isosurface $C_{\omega_{\text{tangential}}}$, computed for the radial locations $0.95 < r/R_{\text{p}} < 1$. Installed case simulated with the FB propeller model ($\theta_{\text{b}} = 45°$, $J = 0.7, T_{c_{\text{FB}}} = 0.87$).

distribution for the installed case. The force vectors help understanding how the change in effective α and the consequent leading edge suction peak result in the production of thrust by the duct. Figure 9d presents the instantaneous pressure coefficient contours on the inner surface of the circular duct for $\theta_{\text{b}} = 45^{\text{o}}$ in the installed configuration. Figures 9a and 9d show that, due to the interaction with the propeller, the lower pressure is lowered everywhere along the leading edge of the duct, more prominently closer to the propeller blade. Furthermore, Fig. 9d also indicates the presence of a strip of lower pressure at the duct surface, trailing from the blade tip. Figure 9e shows the axial skin friction coefficient contours in the inner surface of the circular duct, for the same blade position. At the location of the region of lower C_p (Fig. 9d), a region of negative C_{f_x} is also present, which indicates reversed flow. Therefore, the results indicate that, near the blade tip, the strong pressure jump across the blade causes flow separation in the axial direction at the duct's surface. The pressure jump at the blade also causes a blade tip vortex, which can be seen in Fig. 9f, where an isosurface of constant tangential vorticity coefficient, $C_{\omega_{\text{tangential}}} = C_{\omega_z} \cos\theta + C_{\omega_y} \sin\theta = 15$, is shown for the radial locations $0.95 < r/R_{\text{p}} < 1$. This isosurface reveals the presence of the blade tip vortex. The results indicate that the blade tip vortex continues to interact with the duct's BL after the blade has passed, causing the reversed flow and low static pressure line at the duct's surface. However, since the chordwise length of the reversed flow region is relatively short, this phenomenon does not have a strong effect in the propulsive performance of the system. The dominant effect of the propeller on duct performance is, therefore, the the increased leading-edge suction. The drag produced by the duct is further reduced because the propeller is placed at the position of maximum thickness. Therefore, the increased pressure behind the propeller blades, visible in Fig. 9d, acts on a backwards-facing surface, while the increased suction ahead of the propeller acts on a forwards-facing surface. This phenomenon, discussed previously e.g. in Ref. [38], leads to an additional net axial force which increases duct thrust.

B. Square Duct

The flowfield generated by the square ducted propeller is more complex than the flowfield of the circular ducted propeller case, since the geometry is no longer axisymmetric. Therefore, the steady results (from the AD simulation) are analyzed first in Sec. IV.B.1. Afterwards, the results of the FB simulation are presented in order to understand which additional unsteady phenomena occur (Sec. IV.B.2).

1. Time-Averaged Effects (AD Simulation)

The steady results of the installed square duct simulation are important to understand the effect of the corners on the performance of the system. In this section, the installed AD square duct results are compared against the isolated square duct results. Figure 10a shows the C_{f_x} contours on the inner surface of the isolated square duct. The figure shows a small region of reverse flow ($C_{f_x} < 0$) in the vicinity of the duct's corner. The reverse flow at the duct's surface is an indicator of flow separation. The corners of the square duct were already expected to be prone to separation, as literature indicates that corner boundary layers have a higher thickness, which results in a lower skin friction [13]. Besides, the shape of the square duct was not optimized to prevent this phenomenon. Flow separation can have negative effects in the performance of the system, by increasing the pressure drag of the duct at the corner. Figure 10d shows that, for the installed simulation, the region of reverse flow is considerably larger, starting approximately at the axial position of the propeller, 30% duct chord. For the isolated simulation, identifying the influence of the reversed flow region in the C_p distribution (Fig. 10b) is difficult. On the other hand, Fig. 10e clearly shows that, for the installed case, the static pressure recovers to higher values at the trailing edge for the spanwise locations far from the corner. This result indicates that the separation phenomenon previously identified indeed decreases the performance of the installed system, by increasing pressure drag at the corner. Furthermore, Fig. 10e shows two regions of low C_p located symmetrically on either side of the corner, at the duct's trailing edge. Low C_p can be an indicator of the presence of a vortex. To further investigate this phenomenon, surface streamlines (estimated based on the direction of the skin friction) were drawn on the inner surface of the square duct. Figures 10c and 10f show these surface streamlines, over the C_p contours, for the isolated and installed cases, respectively. In the installed case, the surface streamlines show a curl of the flow surrounding the two symmetric regions of low C_p, which is also an indicator of the presence of vortices. Literature also indicates that corners can be prone to the formation of vortices. Rubin and Grossman [13], who studied the flow over at the corner between two flat plates and also found "swirling flow in the corner", even though in their results "a closed vortical pattern is not established". The surface streamlines pattern observed in Figs. 10c and 10f is also comparable to the flow separation that occurs at wing-body junctions at higher angles of attack [39], although the effective increase in angle of attack is, in this case, a consequence of slipstream contraction.

In order to further investigate the flowfield at the square duct's corner, the flow's axial vorticity is shown in Fig. 11 for three planes: $x/c = 0.3$ (plane of the propeller disk), $x/c = 1$ (at the duct's trailing edge) and $x/c = 1.5$ (downstream of the duct). The axial vorticity is normalised with 2Ω, where Ω is the angular velocity of the propeller at the selected advance ratio ($J = 0.7$). In Fig. 11, the in-plane velocity vectors are also shown. The uninstalled vorticity contours indicate that the axial vorticity in the duct's boundary layer grows towards the trailing edge, which is associated with a minor spanwise movement of the flow towards (inner surface) or away from (outer surface) the corner. This is caused by the increased suction on the inside of the corner of the duct (see Fig. 10b), and reduced suction on the outside of the corner due to 3D-relief effects. Figure 11b also shows the influence of the small separated region at the corner in the vorticity distribution, although in the wake of the system (Fig. 11c), no significant swirl is observed.

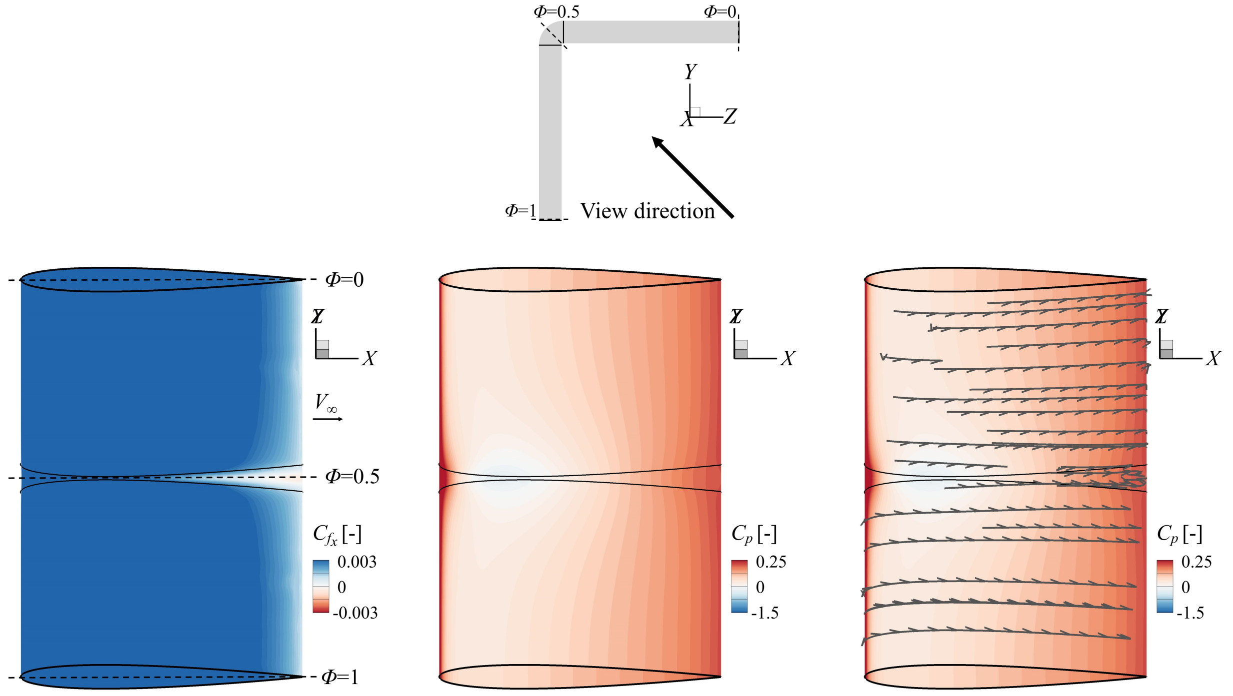

(a) Uninstalled, C_{f_x}

(b) Uninstalled, C_p

(c) Uninstalled, C_p and surface streamlines

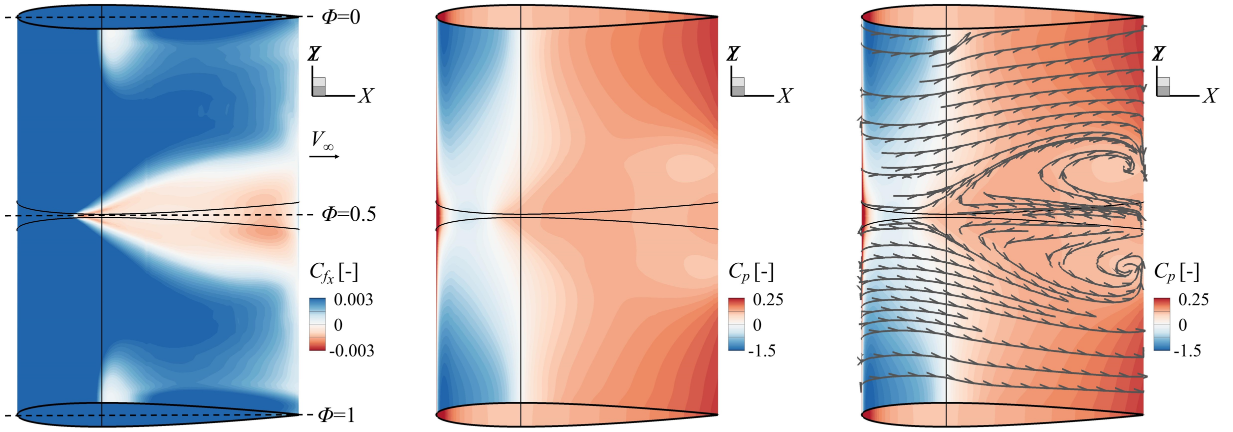

(d) Installed, C_{f_x}

(e) Installed, C_p

(f) Installed, C_p and surface streamlines

Fig. 10 Axial skin friction (left) and pressure (center) coefficient contours, including surface streamlines (right) on the square duct's inner surface. Uninstalled case (top) and installed case (bottom) simulated with AD propeller model ($J = 0.7, T_{c_{\mathrm{AD}}} = 1.13$).

When the propeller is installed, several additional phenomena are visible. Firstly, Fig. 11d shows the swirl imposed by the AD. This leads to a generation of axial vorticity at the inner and outer radius of the AD model, due to the shear that occurs with the surrounding flow. In practice, this vorticity is concentrated in the root and tip vortices of the propeller, respectively. Figure 11d also shows a significant slipstream contraction at the location of the actuator disk, as the velocity vectors are directed away from the corner, in the direction of the AD. This effect can, in fact, contribute towards the strong separation which occurs inside the square duct under these operating conditions, as shown in Figs. 11e and 11f. These figures show how, towards the trailing edge, there is a spanwise flow along the duct surface towards the corners, as had been observed in Fig. 10f. Near the corner, flow reversal occurs (see Fig. 10f), and the flow separates from the wall, moving inwards towards the propeller axis along the bisector of the duct quadrant. Consequently, downstream of the duct (Fig. 11f), two distinct regions of concentrated vorticity of opposite sign are observed. Therefore, both Figs. 10 and 11 indicate the generation of vortices by the square ducted propeller. This phenomenon constitutes a disadvantage of the square duct, as the vortices also contribute towards a higher pressure drag of the system.

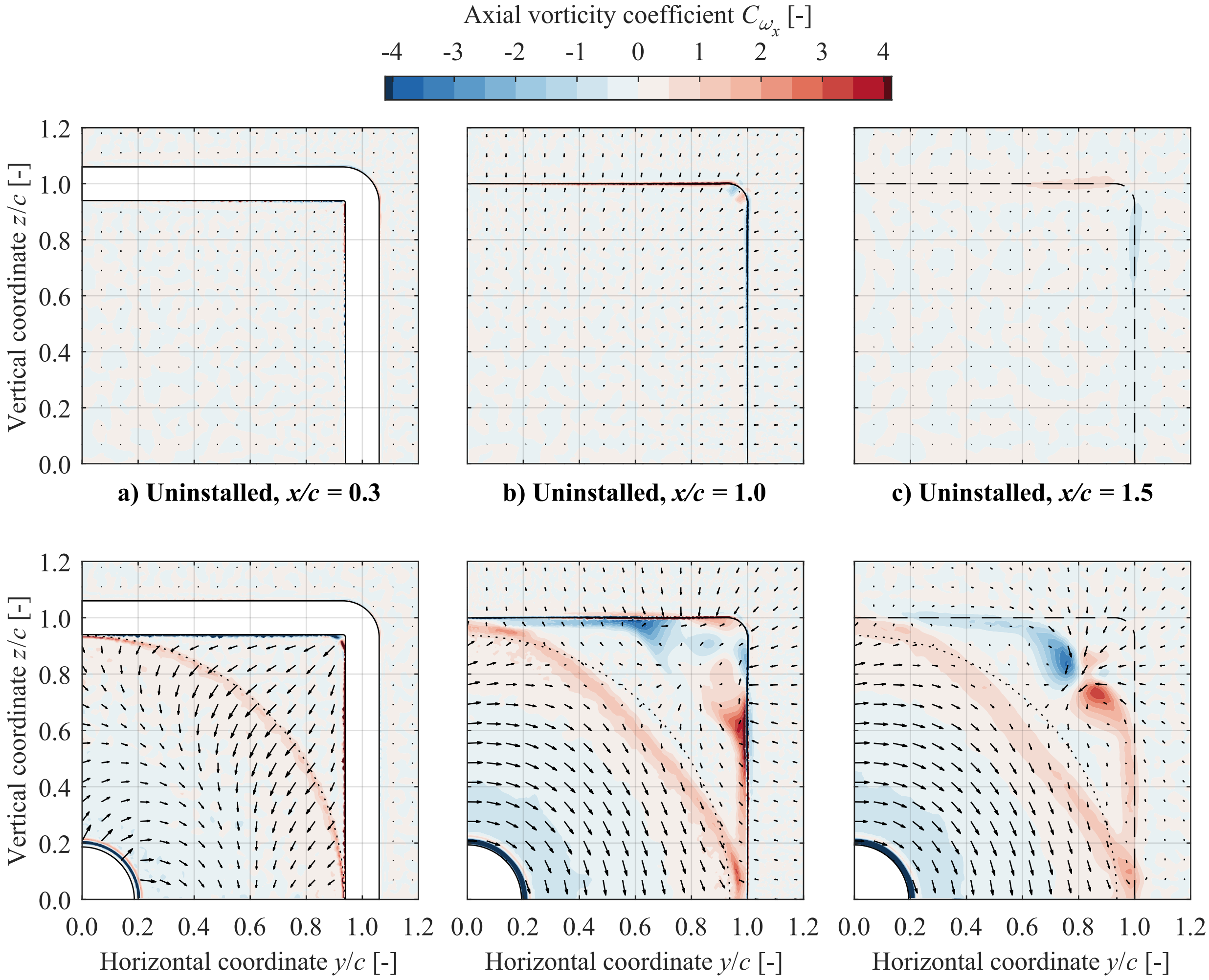

a) Uninstalled, x/c = 0.3

b) Uninstalled, x/c = 1.0

c) Uninstalled, x/c = 1.5

d) Installed, x/c = 0.3

e) Installed, x/c = 1.0

f) Installed, x/c = 1.5

Fig. 11 Axial vorticity contours and in-plane velocity vectors around the corner of the square duct, obtained at the propeller-disk plane (left), duct trailing edge (center), and downstream of the duct (right). Installed case (bottm) simulated with AD propeller model (J = 0.7, $T_{c_{\mathrm{AD}}}$ = 1.13).

2. *Unsteady Effects (Full-Blade Simulation)*

Since the corner vortices can have a strong detrimental effect on the performance of the square ducted system, it is important to analyze how this phenomenon is affected by the unsteady excitation of the propeller blades. Figure 12 shows axial vorticity coefficient, C_{ω_x}, isosurfaces for the installed simulations with the AD (Fig. 12a) and with the FB model (Fig. 12b). Figure 12 shows that the corner vortices generated in the AD simulation are also present in the FB case, although they appear to be weaker. This is an artifact of the lower thrust of the FB with respect to the thrust of the AD model, at the same advance ratio. The thrust of the AD was set to be equal to the thrust of the isolated propeller for each of the three advance ratios considered. The differences in thrust between the isolated and ducted propeller cases are discussed with more detail in the next section. Figure 12a also shows streaks of increased positive vorticity generated near the mid-section of each duct edge. This vorticity is a consequence of the high shear that occurs between the slipstream edge and the duct boundary-layer. In an unsteady sense (Fig. 12b), this region of increased vorticity manifests itself as periodic patches of increased vorticity, generated during each blade passage. Figure 12b also shows the tip vortices present in the propeller slipstream, although they do not form clear helical filaments as occurs for unshrouded propellers. This is due to the cyclic loading that the blade undergoes every 90°, as discussed in the following section.

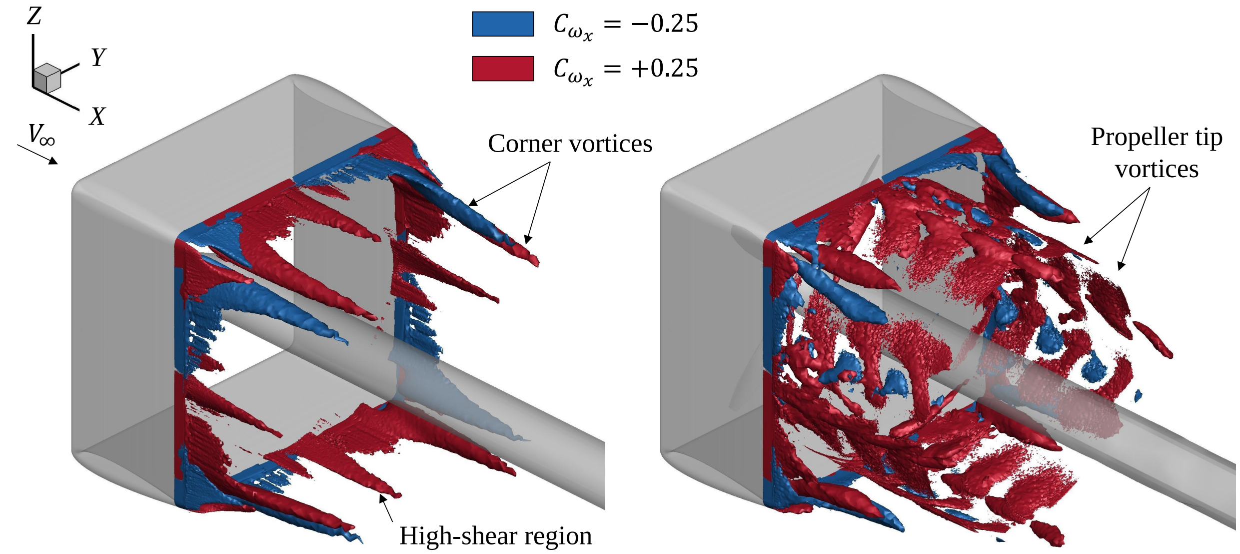

a) AD propeller model **b) FB propeller model**

Fig. 12 Axial vorticity coefficient isosurfaces from the installed square duct simulations ($J = 0.7$), with AD (left) and FB (right) models. Isosurfaces are only shown for axial locations downstream of the duct trailing edge ($x/c > 1$), and for $r/R_\mathrm{p} > 0.5$.

V. Installed System Performance

After having analyzed the main aerodynamic interaction phenomena present in the ducted propeller systems, the main performance parameters are discussed for the different cases. First, the loading distributions on the propeller are presented in Sec. V.A. Then, in Sec. V.B, the loading distributions on the ducts are presented. Finally, Sec. V.C discusses the overall system performance.

A. Blade Loading Distributions

The radial thrust and torque distributions over a propeller blade obtained from the FB simulations are shown in Fig. 16. For the ducted propeller simulations, Fig. 16 shows both the average and the spread of the radial distributions considering all the recorded time steps. The average distributions reveal that the propeller operates at a higher loading for the isolated case, followed by the square duct case. The propeller therefore operates at the lowest loading when installed with the circular duct. The main reason for the differences in averaged thrust and torque are the inflow velocities at the propeller disk. The effective inflow velocity is highest for the circular duct, since the circular duct causes a higher contraction of the streamtube passing through the duct than the square duct, for the same duct airfoil thickness. The effective inflow velocity is lowest for the isolated propeller, which perceives undisturbed free-stream flow. However, near the blade tip ($r/R_\mathrm{p} \rightarrow 1$), the circular ducted propeller generates the highest thrust and torque. This is due to the constant low tip-clearance for the circular ducted propeller. The low tip clearance reduces the tip loss effect and the strength of the blade tip-vortex, thus increasing the loading at large radial locations.

A comparison of the spread of the thrust and torque distributions for the two ducted cases reveals that the radial variations of T and Q are signficant for the square ducted propeller, while practically no variations in loading can be observed for the circular duct, as expected. In the square duct, the propeller blade experiences significant loading variations for two reasons. Firstly, of the inflow velocities at the propeller disk location depend on the azimuthal position of the blade, since the blockage effect of the duct is not axisymmetric. Secondly, the tip clearance of the blade is not uniform inside the square duct, which leads to temporal variations of the tip-loss reduction felt by the propeller blade. Consequently, the variations in blade loading are highest near the tip and, while on average the blade tip-loading is highest for the circular duct, for determined phase angles, the tip-loading is higher in the square duct. This is detrimental for both the noise emissions and fatigue life of the propeller.

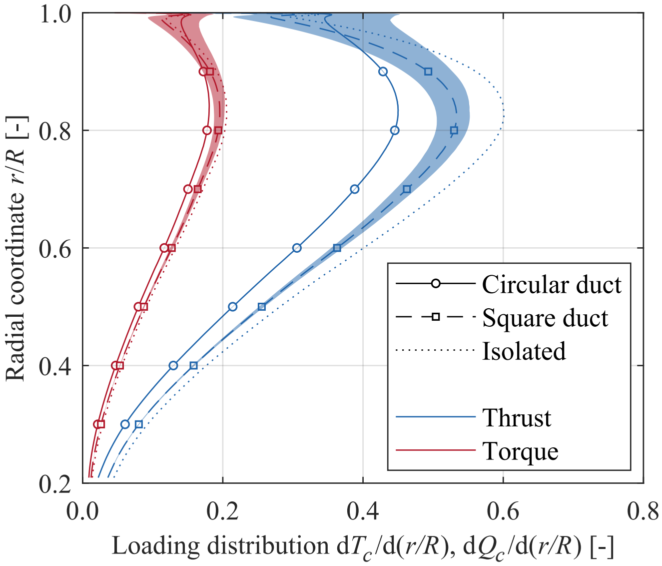

Fig. 13 Radial propeller loading distributions in the isolated and installed (FB) configurations, with the propeller operating at $J = 0.7$. Shaded area indicates the spread in loading throughout a propeller revolution.

B. Duct Loading Distributions

The spanwise distributions of thrust at the circular and square ducts, from the installed FB simulations, were analyzed in order to understand which configuration enables a better propulsive performance of the duct. Figure 14 shows the thrust coefficient distributions along the duct perimeter. The thrust coefficient, T_c, is decomposed into a pressure contribution, T_{c_p}, and a friction contribution, T_{c_f}. In Fig. 14a, which presents the circular duct, the distributions are show versus the azimuthal coordinate of the duct section with respect to the nearest blade. The figure indicates that T_{c_f} is approximately constant with respect to the spanwise location, whereas T_{c_p} sees large variations. T_{c_p} is largest for the duct sections near the blade, which was already expected from the previous analysis of Fig. 9d. Furthermore, Fig. 14a also indicates that, in a reference frame that rotates with the propeller, the temporal variation of the spanwise distributions of thrust at the duct is relatively small.

Figure 14b shows the thrust distributions for the square duct with respect to the spanwise location ϕ. The figure indicates that the spanwise variation of the friction thrust coefficient is also smaller than the spanwise variation of the pressure thrust coefficient for the square duct. Still, T_{c_f} is higher (less negative) at the corner, where $\phi = 0.5$, than for spanwise locations far from the corner. This is due to the reverse flow region near the corner, identified previously in Fig. 10d. Figure 14b also shows that the temporal variation of T_{c_f} for each duct section is negligible, which indicates that the flow separation in the corner does not vary significantly with the blade position. In other words, the increased separation in the corner of the duct is a consequence of the slipstream contraction observed in Fig. 11, and not an unsteady phenomenon which is excited at the blade-passage frequency. The T_{c_p} distribution, on the other hand, shows large fluctuations with the periodic passage of the propeller blades. On average, the duct produces more pressure thrust at the locations far from the corner. Towards the corner of the square duct, T_{c_p} reduces due to two main reasons. Firstly, due to the larger distance between the corner sections and the propeller disk, the effect of slipstream contraction on the

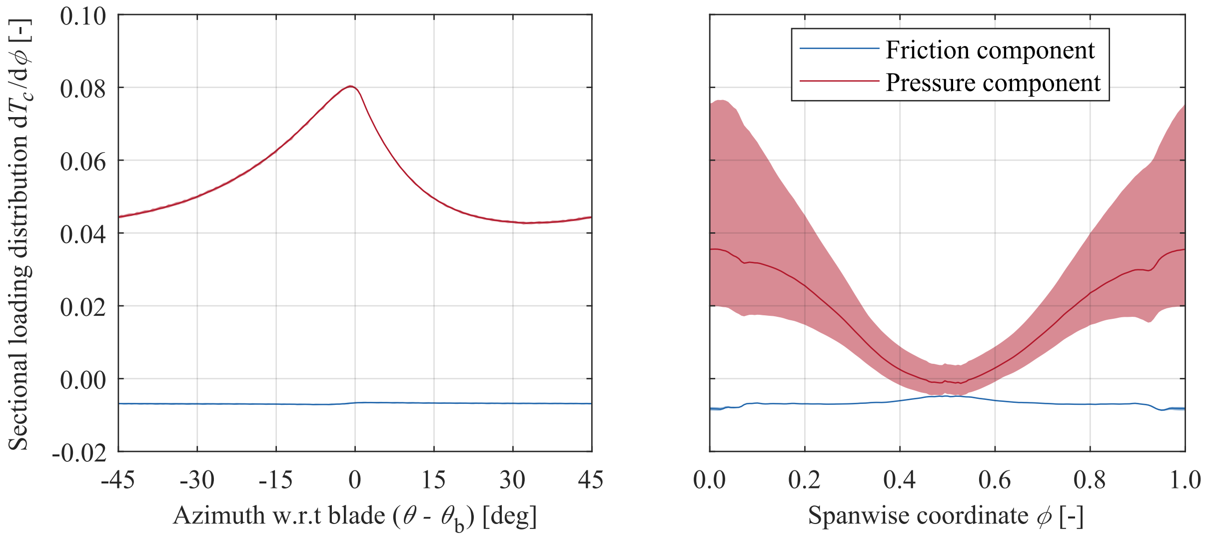

a) Circular duct **b) Square duct**

Fig. 14 Spanwise thrust coefficient distributions along the duct perimeter in the installed configurations (FB, J = 0.7. Shaded area indicates the spread in loading throughout a propeller revolution. Note that the x-axes are expressed in the propeller and duct reference frame for subplots (a) and (b), respectively.

local angle of attack perceived by the corner sections reduces. Secondly, the corner's axial flow separation and the associated corner vortices also contribute towards the generation of drag at the duct. The comparison of Figs. 14a and 14b also indicate that the circular duct is able to produce more thrust than the square duct, for the same rotational speed of the propeller, even though the propeller itself produces more thrust when placed inside the square duct.

C. System Thrust and Efficiency

In this section, the loading distributions are integrated to understand how the thrust produced by the different systems compares, as well as their efficiency. For the installed systems, efficiency was defined as $\eta = V_\infty(T_\mathrm{p} + T_\mathrm{duct})/P_\mathrm{shaft}$. Firstly, Fig. 15 shows the ratio of duct thrust to system thrust obtained from the installed AD simulations, for both ducts and for the three operating conditions tested, $J = 0.9$, $J = 0.8$ and $J = 0.7$. The figure indicates that both ducts are able to contribute more towards the system's thrust as the system's thrust setting increases, i.e., as J decreases. This is due to the higher slipstream contraction that is perceived by the duct when the thrust setting increases. Besides, Fig. 15 also shows that the thrust of the circular duct with respect to the system's thrust is higher than the square duct's contribution, for all operating conditions tested. This result is consistent with the discussion of the previous section. Note that, at the lowest thrust setting evaluated, the square duct produces negative thrust. In other words, at low thrust settings, the pressure drag in the corners of the duct and friction drag outweigh the suction generated on the leading edge due to slipstream contraction.

Finally, Fig. 16 shows the time-averaged thrust coefficient and efficiency of the three systems studied with the FB propeller model: the isolated propeller, circular ducted propeller and square ducted propeller. Figure 16 shows that the isolated propeller is the propulsion system which produces more thrust, for the chosen advance ratio. The main reason for this is the lower axial velocity of the flow at the propeller disk, when compared to the ducted configurations. However, even though the isolated propeller produces the highest thrust, the efficiency of the isolated propeller is lower than the efficiency of the circular ducted system. This is primarily because the isolated propeller operates at a lower effective advance ratio than in the circular duct, and therefore operates at a less optimal point along the efficiency curve of the propeller.

As discussed previously, the propeller produces more thrust inside the square duct than inside the circular duct (at a fixed J setting), whereas the circular duct produces the more thrust than the square one. At the operating conditions tested, both ducted systems produce the same net thrust (with a difference of only 0.4%), as visible in Fig. 16. At the same system thrust, the circular ducted propeller is estimated to be 4.5% more efficient than the square ducted propeller. However, this value has to be interpreted with caution since, for the same system thrust, the propeller produces more

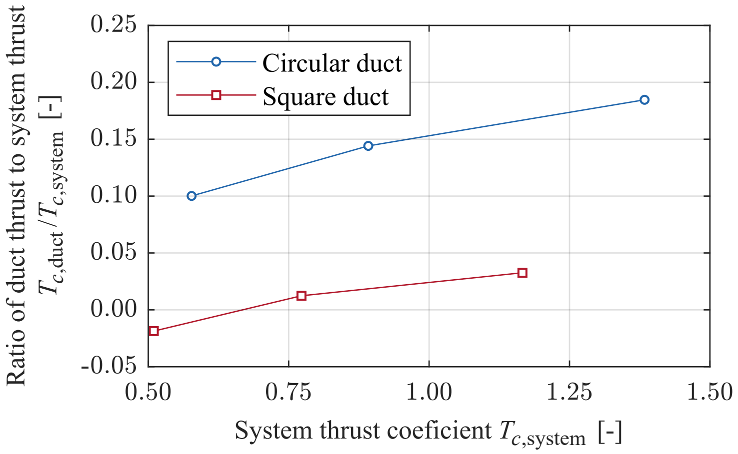

Fig. 15 Ratio of duct thrust to total system (i.e., propeller + duct) thrust obtained from the AD simulations for three propeller thrust settings (J = 0.7, $T_{c_{\text{AD}}}$ = 1.13; J = 0.8, $T_{c_{\text{AD}}}$ = 0.76; and J = 0.9, $T_{c_{\text{AD}}}$ = 0.52).

thrust inside the square duct. This occurs because the propeller operates at a lower effective advance ratio, since the average inflow velocity to the propeller disk is lower for the square duct than for the circular duct. Therefore, it is at a less efficient operating point along its efficiency curve (see Fig. 8c), and for a fair comparison, the blade pitch of both ducted systems would have to be adapted to maximize efficiency at the same total system thrust. This would decrease the efficiency penalty of the square ducted system. In any case, the aerodynamic phenomena discussed in the previous sections confirm that, for a single propeller, a circular ducted system is more efficient than a square one.

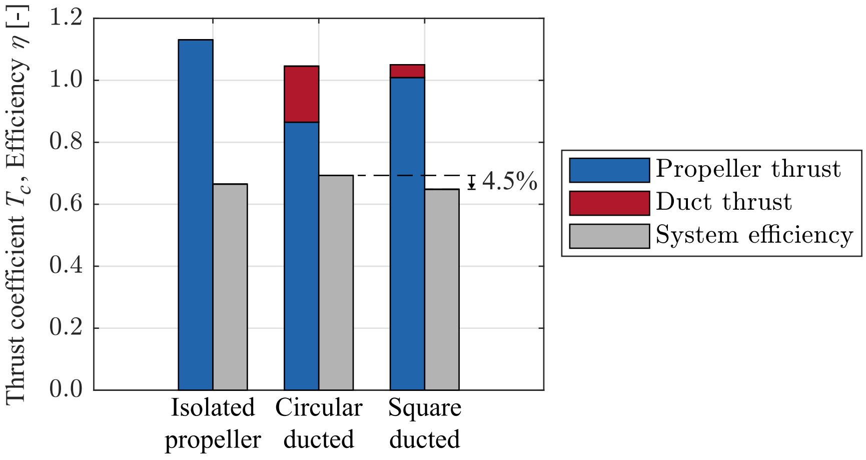

Fig. 16 Thrust coefficient and system efficiency of the three propulsion systems, obtained from the FB model for J = 0.7.

VI. Conclusions and Outlook

CFD simulations have been performed in order to understand the main aerodynamic differences between two propulsive systems: a circular ducted propeller, which constitutes the reference case, and a square ducted propeller, which represents an idealized unconventional duct design. The aerodynamic interaction effects occurring in both ducts were analysed so that the differences in aerodynamic performance could be understood. The operating condiditions were selected such that the rotational speed of the propeller would result in a high thrust setting. At a high thrust setting, the propeller causes a stronger slipstream contraction upstream of the duct, which is then responsible for the production of thrust by the duct.

For the same advance ratio, the circular duct is found to generate more thrust than the square duct. This occurs due to two main reasons. Firstly, in the circular duct configuration the propeller is always close to the duct surface, which means that the slipstream contraction caused by the propeller has a strong effect on the loads on the circular duct. On the other hand, for the square duct case, the propeller blades have a weaker effect on the performance of the duct when these are pointing at the corner, due to the larger distance between blades and duct surface. Secondly, the corner of the square duct results in adverse aerodynamic effects. In the installed configurations, separation occurs at the corner, and this phenomenon is associated with the generation of corner vortices. However, the propeller produces more thrust inside the square duct than inside the circular duct, for the same advance ratio. This is due to a lower axial inflow velocity at the propeller disk inside the square duct. The non-axisymmetric inflow inside the square duct also leads to significant cyclic loading variations on the propeller blades. The higher thrust of the propeller when placed inside the square duct compensates for the lower generation of thrust by the square duct. Thus, at the operating conditions tested, both the circular and the square ducted propeller propulsion systems were found to produce the same thrust. In these conditions, the efficiency of the circular ducted propeller is approximately 4.5% higher than the efficiency of the square ducted propeller.

However, the propulsive efficiency penalty of the square duct should not discourage research on these propulsion systems, especially since it can already be reduced by selecting the appropriate blade pitch setting. For future study, it is recommenced that the circular and square ducted propellers are studied at different rotational speeds and blade pitch settings, to obtain representative performance curves at system level. Besides, studying square duct geometries with increasing corner radius—the limit case of which is a circular duct—would help understand how the adverse corner flow effects can be mitigated. Furthermore, future studies should also focus on the comparison between distributed-propulsion systems with arrays of circular and square ducted propellers. Even though the present study indicates aerodynamic disadvantages of square ducts when considering an isolated propeller, the lower wetted area of an array of square ducts, when compared to an array of circular ducts, may lead to different conclusions when multiple adjacent rotors are considered. Moreover, the uncertainty analysis of this paper shows that such studies should, at least partially, involve experimental investigations, in order to properly validate the numerical methods and increase the confidence in results. This will enable a thorough understanding of the aerodynamic performance of ducted rotors, which is an essential step towards the development of novel, highly integrated propulsion systems

Acknowledgments

The authors would like to thank Nando van Arnhem and Tom Stokkermans for their help with the CFD simulations. Their expertise was essential for the research. The authors would also like to thank Tomas Sinnige for providing the wind-tunnel data on the performance of the isolated propeller.

References

[1] Black, D.M., Wainauski, H.S., and Rohrbach, C., “Shrouded propellers - A comprehensive performance study,” *AIAA 5th Annual Meeting and Technical Display*, 1968. doi:10.2514/6.1968-994.

[2] Bogdański, K., Krusz, W., Rodzewicz, M., and Rutkowski, M., “Design and optimization of low speed ducted fan for a new generation of joined wing aircraft,” *29th Congress of International Council of the Aeronautical Sciences*, Saint Petersburg, 2014.

[3] Williams, M.H., Cho, J., and Dalton, W.N., “Unsteady aerodynamic analysis of ducted fans,” *Journal of Propulsion and Power*, Vol. 7, No. 5, 1991, pp. 800–804. doi:10.2514/3.23394.

[4] Pereira, J.L., “Hover and wind-tunnel testing of shrouded rotors for improved micro-air vehicle design,” Ph.D. thesis, University of Maryland, College Park, 2008.

[5] Hubbard, H.H., “Sound measurements for five shrouded propellers at static conditions,” Tech. Rep. NACA-TN-2024, National Advisory Committee for Aeronautics, 1950.

[6] Vos, R., and Hoogreef, M.F.M., “System-level assessment of tail-mounted propellers for regional aircraft,” *31st Congress of the International Council of Aeronautical Sciences*, Belo Horizonte, Brazil, 2018.

[7] Kim, H.D., “Distributed Propulsion Vehicles,” *27th Congress of the International Council of the Aeronautical Sciences*, Nice, France, 2010.

[8] Steiner, H. J., Seitz, A., Wieczorek, K., Plötner, K., Iskiveren, A. T., and Hornung, M., "Multi-disciplinary design and feasibility study of distributed propulsion systems," *28th Congress of the International Council of the Aeronautical Sciences*, Brisbane, Australia, 2012.

[9] de Vries, R., Hoogreef, M.F.M., and Vos, R., "Preliminary Sizing of a Hybrid-Electric Passenger Aircraft Featuring Over-the-Wing Distributed-Propulsion," *2019 AIAA Aerospace Sciences Meeting*, San Diego, CA, USA, 2019. doi:10.2514/6.2019-1811.

[10] Schmollgruber, P., Döll, C., Hermetz, J., Liaboeuf, R., Ridel, M., Cafarelli, I., Atinault, O., François, C., and Paluch, B., "Multidisciplinary Exploration of DRAGON: an ONERA Hybrid Electric Distributed Propulsion Concept," *2019 AIAA Aerospace Sciences Meeting*, San Diego, CA, USA, 2019.

[11] Felder, J. L., Kim, H. D., and Brown, G. V., "Turboelectric Distributed Propulsion Engine Cycle Analysis for Hybrid-Wing-Body Aircraft," *47th AIAA Aerospace Sciences Meeting*, Orlando, FL, USA, 2009.

[12] Electric VTOL News by the Vertical Flight Society, "Lilium Jet," , accessed November 2019. URL `https://evtol.news/aircraft/lilium/`.

[13] Rubin, S., and Grossman, B., "Viscous flow along a corner: numerical solution of the corner layer equations," *Quarterly of applied mathematics*, 1971.

[14] Tokuda, N., "Viscous flow near a corner in three dimensions," *Journal of Fluid Mechanics*, Vol. 53, No. 1, 1972, pp. 129–148.

[15] Li, Q., "Towards optimum swirl recovery for propeller propulsion systems," Ph.D. thesis, Delft University of Technology, Delft, 2019.

[16] de Vries, R., van Arnhem, N., Avallone, F., Ragni, D., Vos, R., Eitelberg, G., and Veldhuis, L. L. M., "Aerodynamic Interaction Between an Over-the-Wing Propeller and the Wing Boundary-Layer in Adverse Pressure Gradients," *2019 AIAA Aviation Technology, Integration and Operations Conference*, Dallas, TX, USA, 2019.

[17] van Arnhem, N., de Vries, R., Vos, R., and Veldhuis, L. L. M., "Aerodynamic Performance of an Aircraft Equipped with Horizontal Tail Mounted Propellers," *2019 AIAA Aviation Technology, Integration and Operations Conference*, Dallas, TX, USA, 2019.

[18] van Arnhem, N., Vos, R., and Veldhuis, L.L.M., "Aerodynamic Loads on an Aft-Mounted Propeller Induced by the Wing Wake," *2019 AIAA Aerospace Sciences Meeting*, San Diego, CA, USA, 2019.

[19] Küchemann, D., and Weber, J., *Aerodynamics of Propulsion*, McGraw-Hill, 1953.

[20] ANSYS Fluent, "12.0 Theory Guide," , 2009. Ansys Inc.

[21] van Leer, B., "Towards the Ultimate Conservative Difference Scheme. V. A Second-Order Sequel to Godunov's Method," *Journal of Computational Physics*, Vol. 32, No. 1, 1979. doi:10.1016/0021-9991(79)90145-1.

[22] Menter, F.R., "Two-Equation Eddy-Viscosity Turbulence Models for Engineering Applications," *AIAA Journal*, Vol. 32, No. 8, 1994, pp. 1598–1605. doi:10.2514/3.12149.

[23] Ortun, B., Boisard, R., and Gonzalez-Martino, I., "In-plane airloads of a propeller with inflow angle: prediction vs. experiment," *30th AIAA Applied Aerodynamics Conference*, 2012. doi:10.2514/6.2012-2778.

[24] Falissard, F., Boisard, R., and Delattre, G., "Aeroacoustic computation of a contra rotating open rotor model with test rig installation effects," *18th AIAA/CEAS Aeroacoustics Conference (33rd AIAA Aeroacoustics Conference)*, 2012. doi:10.2514/6.2012-2218.

[25] Méheut, M., "Thrust and Torque Far-field Analysis of Propeller and Counter Rotating Open Rotor Configurations," *31st AIAA Applied Aerodynamics Conference*, 2013. doi:10.2514/6.2013-2803.

[26] Ruiz-Calavera, L.P., and Perdones-Diaz, D., "CFD computation of in-plane propeller shaft loads," *AIAA/ASME/SAE/ASEE Joint Propulsion Conference*, 2013. doi:DOI:10.2514/6.2013-3798.

[27] Bardina, J., Huang, P., and Coakley, T., "Turbulence modeling validation," *In 28th Fluid dynamics conference*, 1997. doi:10.2514/6.1997-2121.

[28] Mannini, C., Soda, A., and Schewe, G., "Unsteady RANS modelling of flow past a rectangular cylinder: Investigation of Reynolds number effects," *Computers & fluids*, Vol. 39, No. 9, 2010. doi:10.1016/j.compfluid.2010.05.014.

[29] Stokkermans, T.C.A., van Arnhem, N., Sinnige, T., and Veldhuis, L., “Validation and Comparison of RANS Propeller Modeling Methods for Tip-Mounted Applications,” *AIAA Journal*, Vol. 57, No. 2, 2019, pp. 566–580. doi:10.2514/1.J057398.

[30] Spalart, P.R., and Rumsey, C.L., “Effective Inflow Conditions for Turbulence Models in Aerodynamic Calculations,” *AIAA Journal*, Vol. 45, No. 10, 2007, pp. 2544–2553. doi:10.2514/1.29373.

[31] Bento, H.F.M., “Aerodynamic interaction effects of circular and square ducted propellers,” Msc thesis, Delft University of Technology, Delft, The Netherlands, May 2019.

[32] Eça, L., and Hoekstra, M., “Discretization Uncertainty Estimation Based on a Least Squares Version of the Grid Convergence Index,” *Proceedings of the Second Workshop on CFD Uncertainty Analysis, Instituto Superior Técnico, Lisbon, Oct.*, 2006.

[33] Jacobs, E.N., and Sherman, A., “Airfoil section characteristics as affected by variations of the Reynolds number,” Tech. Rep. NACA-TR-586, NASA, 1937.

[34] Traub, L.W., “Preliminary Investigation of the Effects of Stagger on an Annular Wing,” *Journal of Aircraft*, Vol. 54, No. 6, 2017, pp. 2386–2392. doi:10.2514/1.C034310.

[35] Sinnige, T., “Aerodynamic and Aeroacoustic Interaction Effects for Tip-Mounted Propellers,” Ph.D. thesis, Delft University of Technology, Delft, 2018.

[36] Drela, M., and Youngren, M., “XROTOR Download Page,” , acessed November 2013. URL `http://web.mit.edu/drela/Public/web/xrotor/`.

[37] Drela, M., “XFOIL: An analysis and design system for low Reynolds number airfoils,” *Low Reynolds number aerodynamics*, Springer, 1989, pp. 1–12.

[38] Marcus, E.A.P., de Vries, R., Kulkarni, A.R., and Veldhuis, L.L.M., “Aerodynamic Investigation of an Over-the-Wing Propeller for Distributed Propulsion,” *2018 AIAA Aerospace Sciences Meeting*, Kissimmee, FL, USA, 2018. doi:10.2514/6.2018-2053.

[39] Gand, F., Monnier, J.C., Deluc, J.M., and Choffat, A., “Experimental Study of the Corner Flow Separation on a Simplified Junction,” *AIAA Journal*, Vol. 53, No. 10, 2015, pp. 2869–2877.